promoting access to White Rose research papers

Universities of Leeds, Sheffield and York
http://eprints.whiterose.ac.uk/

This is a copy of the final published version of a paper published via gold open access in **Acta Materialia**.

This open access article is distributed under the terms of the Creative Commons Attribution Licence (http://creativecommons.org/licenses/by/4.0/) which permits unrestricted use, distribution, and reproduction in any medium, provided the original work is properly cited.

White Rose Research Online URL for this paper:
http://eprints.whiterose.ac.uk/86234

Published paper

Mumtaz, K.A., Harrison, N. and todd, I. (2015) *Reduction of micro-cracking in nickel superalloys processed by Selective Laser Melting: A fundamental alloy design approach*. Acta Materialia, 94. 59 - 68 . Doi: 10.1016/j.actamat.2015.04.035

White Rose Research Online
eprints@whiterose.ac.uk

Available online at www.sciencedirect.com

ScienceDirect

Acta Materialia 94 (2015) 59–68

Acta MATERIALIA

www.elsevier.com/locate/actamat

Reduction of micro-cracking in nickel superalloys processed by Selective Laser Melting: A fundamental alloy design approach

Neil J. Harrison,[a] Iain Todd[b] and Kamran Mumtaz[a,*]

[a] *Department of Mechanical Engineering, University of Sheffield, Sheffield, UK*
[b] *Department of Materials Science and Engineering, University of Sheffield, Sheffield, UK*

Received 23 January 2015; revised 30 March 2015; accepted 23 April 2015
Available online 16 May 2015

Abstract—The Selective Laser Melting (SLM) process generates large thermal gradients during rapid melting of metallic powdered feedstock. During solidification certain alloys suffer from thermally induced micro-cracking which cannot be eliminated by process optimisation. An alloy's crack susceptibility may reduce by increasing its Thermal Shock Resistance (TSR), potentially achieved through an increase in tensile strength. This hypothesis is investigated with Hastelloy X, a common nickel-base superalloy of known high crack susceptibility when processing SLM. It is demonstrated that through consideration of the imposed rapid solidification conditions, Hastelloy X can be made to form a supersaturated solid solution in the as deposited state. The fundamental solid solution strengthening (SSS) effect is exploited to generate an increase in lattice stress, by increasing the most potent SSS elements present within the alloy, whilst maintaining specification composition. The modified alloy displayed a 65% reduction in cracking and an increase in elevated temperature tensile strength, lending support to the initial hypothesis and identifying a possible approach for developing further SLM crack resistant versions of well-known alloy compositions.
© 2015 Acta Materialia Inc. Published by Elsevier Ltd. This is an open access article under the CC BY license (http://creativecommons.org/licenses/by/4.0/).

Keywords: Selective Laser Melting; Additive Manufacturing; Rapid solidification; Microcracking; Nickel superalloys

1. Introduction

Selective Laser Melting (SLM) is an Additive Manufacturing (AM) process in which metallic powder is selectively melted and fused by a high powered laser. Cross sections of the part are fused in layers, which are built up successively to create the complete 3D object. The method of layered fabrication, combined with the high precision of laser melting allows for a greatly expanded design freedom with minimal feedstock waste.

The technology is greatly applicable for use in high value markets such as the aerospace industry, and in particular for use of high temperature materials such as nickel-base superalloys. The characteristic properties of superalloys (increased hardness and tensile strength) can make them difficult form using conventional techniques; fabricating full density superalloy components using SLM is an area of great interest. One of the main issues preventing the widespread use of SLM to manufacture aerospace components is resultant part integrity, which is hampered by thermally induced residual stress and micro-cracking. Certain nickel-base superalloys have been documented as being particularly susceptible to micro-cracking when processed using SLM [1–3], in reality the number of crack susceptible alloys far exceeds those reported in the public domain.

1.1. Thermal stress and micro-cracking

Mercelis and Kruth [4] described the thermal residual stress found in SLM parts as arising from two mechanisms; Thermal Gradient Mechanism (TGM) and the cool-down phase of molten top layers. In TGM, the rapid heating of the top surface combined with the relatively slow heat conduction of the material, creates a steep temperature gradient. When the top layer expands, it is restricted by the significantly cooler lower layer, inducing elastic compressive strain. However, at an increased temperature the yield strength of the upper layer is reduced, allowing it to be plastically compressed. Cooling of the now plastically compressed upper layer causes it to shrink, inducing a bending angle towards the laser source thus introducing a tensile stress in the build direction. It is important to note that this mechanism occurs in the solid phase, beyond the solidification trace.

The cooling of the molten top layer (shrinkage) induces stress in a similar way to TGM. When the material cools and solidifies it shrinks due to thermal contraction. This shrinkage is again restricted by the cooler underlying material, causing tensile stress in the top layer and compressive stress in the underlying layer.

Both mechanisms can also lead to stress relief through fracturing, if the tensile stress exceeds the Ultimate Tensile Strength (UTS) of the solid material at a given

* Corresponding author; e-mail: k.mumtaz@sheffield.ac.uk

http://dx.doi.org/10.1016/j.actamat.2015.04.035
1359-6462/© 2015 Acta Materialia Inc. Published by Elsevier Ltd.
This is an open access article under the CC BY license (http://creativecommons.org/licenses/by/4.0/).

point and temperature. This solid phase fracturing will be referred to as 'hot cracking', and is not to be confused with solidification/liquation cracking which is as a result of low melting eutectic phase or liquid film at the grain boundary [3].

Micro-cracking and thermal stresses have been reduced through control of laser scanning parameters and heated platforms [1,4–7]. Hot Isostatic Pressing (HIP) can be used to consolidate cracks, however surface cracks and open porosity still remain [8]. In addition, the HIP process leads to coarsening of grains [9,10]. It is therefore argued that laser parameter control and/or post processing are not definitive solutions, and a more universal solution also requires the optimisation of the alloy during processing.

An investigation by Tomus et al. [1] looked into the effects of minor elements, specifically Si and Mn, on the crack susceptibility of Hastelloy X during SLM processing. The hypothesis was that microsegregation of these elements towards the grain boundaries was resulting in weakened/brittle phases, thereby increasing the chance of micro-cracking. The effect was compared to the findings of Savage and Krantz [11] who established it to be a major factor in cracking in autogenous Hastelloy X welds. In Tomus' investigation it was found that in as deposited form, an alloy with a 'high' Si + Mn content displayed more severe cracking than one with a 'low' Si + Mn content, and it was thus concluded that the hypothesis had been supported. However, the nondisclosure of more precise Si + Mn composition and lack of chemical analysis across crack regions make this work inconclusive. Moreover, as will be discussed in Section 3, the solidification rates in SLM are unlikely to allow for this magnitude of solute segregation.

1.2. Thermal stability and thermal shock resistance

Hunt [12] suggests that the 'processable' nature of a metal depends on two performance indicators, thermal stability and Thermal Shock Resistance (TSR). Thermal stability refers to the extent at which a material will deform or deflect for a given heat input and geometry, and is described by the performance indicator κ/α_{CTE}; where κ is thermal conductivity and α_{CTE} is the co-efficient of thermal expansion. TSR refers to a material's ability to resist crack formation as a result of change in temperature, for a given heat input and geometry. The assumption is that 'good thermal stability' refers to minimal deflection, therefore it is preferable to maximise κ/α_{CTE}. For a good TSR (τ) one must maximise Eq. (1), where σ_{UTS} is the UTS (preferred over fracture strength when applying TSR to ductile materials), ν is the Poisson ratio and E is Young's modulus. Yield strength is usually chosen over UTS as it is still desirable for the material to not plastically deform, however for fracture UTS is more applicable.

$$\tau = \frac{\boldsymbol{\sigma_{UTS}} \cdot \boldsymbol{\kappa} \cdot (\mathbf{1} - \boldsymbol{\nu})}{\boldsymbol{E} \cdot \boldsymbol{\alpha_{CTE}}} \tag{1}$$

Work on symmetry relationships between alloy properties [13] finds that α_{CTE} is inversely related to E, as thus the denominator in Eq. (1) becomes ineffectual. It also implies that an attempt to increase thermal stability may have undesired effects on the elastic modulus and mechanical strength of the alloy. In addition, increasing κ will decrease the absorptivity of the alloy as a result of increased free electrons; this is also to be avoided. It is therefore proposed that rather than the two separate performance indicators, we consider the crack susceptibility of an alloy, χ, which is dependent on the ratio $\tau/\sigma_T(T, C_p, \alpha_{CTE})$, where σ_T is the thermal stress and is some function of temperature, T, specific heat capacity, C_p and α_{CTE}. Given the above discussion, this is further reduced to Eq. (2).

$$\chi = \frac{\sigma_{UTS}}{\sigma_T} \tag{2}$$

For a material to withstand hot cracking, the inequality $\sigma_{UTS} > \sigma_T$ must be satisfied, and hence $\chi > 1$. This investigation focuses on affecting σ_{UTS}, as opposed to E, as it poses a lower risk of detrimentally affecting the alloy's mechanical properties.

1.3. Rapid solidification and microstructure

SLM can be treated similarly to laser surface treatment processing, in which there is the rapid movement of a high energy heat source moving with velocity V_b. The characteristic solidification conditions for laser surface processing are outlined by Kurzand Trivedi [14] in their work on Rapid Solidification Processing (RSP). In RSP, microstructure selection is driven by the interface velocity V_s and cooling rate $|\dot{T}|$, and temperature gradient at the interface G is less significant. In laser surface processing, V_s increases rapidly from zero at the base of the melt pool to $\sim V_b$ at the surface via the relationship $V_s = V_b \cdot \cos\theta$, where θ is the angle between the velocities [15], see Fig. 1. Typical laser scan velocities for SLM are between 0.1 and 1 m/s which, using $V_s = V_b \cdot \cos\theta$, leads to V_s of the same magnitude. Despite the rapid acceleration of the solid–liquid interface, steady state growth theory is still applicable; as demonstrated by Zimmerman et al. [16]. Eq. (3) gives the quasi-steady state term for the solidification rate and acceleration.

$$\frac{\frac{D\partial V_S}{V_S \partial x}}{V_S} \ll 1 \tag{3}$$

where D is the diffusion coefficient of the solute in liquid. Taking the maximum value for $(\Delta V_s/\Delta x)$as 10^3–10^4 s^{-1} [16] and taking D to be of the order 10^{-9} m^2/s, the LHS of Eq. (3) has values of 10^{-6}–10^{-3} when applied to SLM solidification rates. The quasi-steady state condition is therefore satisfied, and steady state growth theory can be applied.

Along with additional works [15,17], Kurz and Trivedi determine that solidification conditions for laser surface treatment will in most cases lead to columnar (directional) growth of dendrites, adapted from [14] see Fig. 2. In directional growth $|\dot{T}| = GV$, given G of 10^6 K/m, $|\dot{T}|$ of 10^5 K/s is obtained.

Under high thermal gradients, dendrites form parallel to the heat flux and thus perpendicular to the melt pool/solid interface as shown in Fig. 1. In SLM the dendrites advance through epitaxial growth, as each layer reconsolidates the majority of the previous, resulting in dendrites which transcend multiple layers. The orientation of the dendrites is maintained by the presence of a large heat sink (substrate) which creates a strong heat flux parallel and negative to the build direction. All this culminates in high aspect ratio columnar grains oriented in the build (z) direction [18]; this

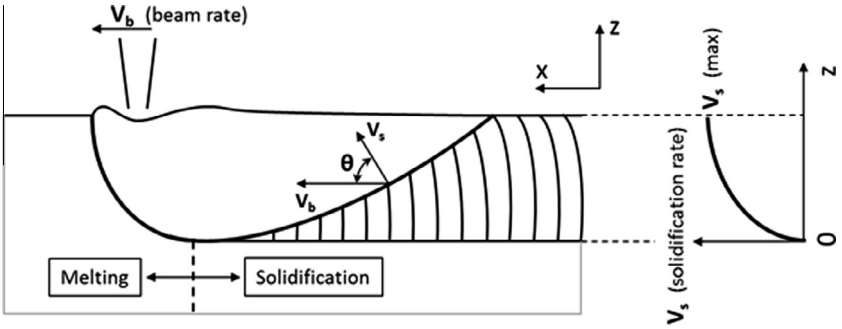

Fig. 1. Melt pool formation for laser surface processing at high beam velocities, adapted from [15]. Where V_s (max) $\equiv V_b$.

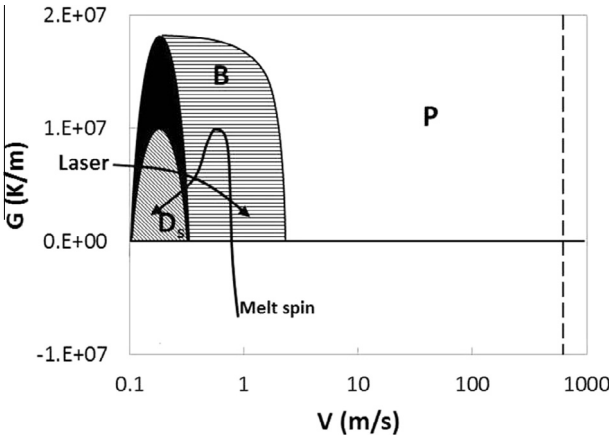

Fig. 2. G–V microstructure selection map, typical values for G and V in SLM are 10^6 K/m and 0.4 m/s respectively. Columnar dendrites are indicated by D_s, banded structure B and planar structure P – adapted from [14].

microstructure has been well documented in SLM investigations [19–22].

Given the proposed solidification conditions it is predicted that $V_s \geqslant D_i/\delta$, where D_i is the interface diffusion coefficient of the solute element (which is less than that for bulk liquid) and δ is the interface width [23], therefore significant solute trapping will occur. If it can be demonstrated that the imposed rapid solidification conditions will result in solute trapping (leading to a super saturated solid solution), Eq. (1) can be maximised by increasing the lattice stress of the alloy through solid solution strengthening alone.

In this investigation a superalloy of known high crack susceptibility, Hastelloy X, is initially processed under optimised conditions to establish minimum crack density. Microstructure and chemical analysis on as deposited samples are used to verify the solidification conditions and the validity of the hypothesis. Gypen and Deruyttere's model for multicomponent solid solution hardening [24] is then used to design a modified version of Hastelloy X with increased lattice strength; with the intention of increasing the TSR of the alloy and reducing micro-crack formation.

2. Experimental procedures

2.1. Sample build and preparation

All samples were fabricated on a Renishaw SLM 125 machine with metallic powder feedstock being supplied by LPW Technology. The Renishaw SLM 125 uses a modulated 200 W Ytterbium fibre laser to process deposited powder feedstock within a 125 × 125 × 125 mm build volume. The modulated laser scans in a point-to-point regime, rather than a continuous scan. The controllable parameters are set as point distance and exposure time, where point distance is the distance between each fusion point and exposure time is the time the laser remains on each point; together they combine to produce an apparent velocity which is more comparable with a standard continuous laser. A meander scan strategy (raster with 67° rotation for each layer) was used for all trials as it has been optimised to minimise part residual stress. Other controllable parameters are laser power, hatch spacing and layer thickness.

The nominal composition of Hastelloy X is detailed in Table 1, along with the actual composition of the Unmodified Original Hastelloy X (OHX) version; the spherical powder feedstock was sized at 15–45 μm. Samples were initially built as 10 × 10 × 10 mm samples for the parameter optimisation trial (Section 3.1). There was a limited volume of the modified alloy powder available as it was a special atomisation run. Sample size was therefore reduced to 5 × 5 × 5 mm for alloy comparison trials (Sections 4.2 and 4.3) in order to maximise sample population.

Chemical analysis of the powders was conducted by LSM International using bead fusion and analysis on a wavelength dispersive XRF. Tensile bars were built as cuboids and then machined down to ASTM E21 2009 round specimen; 6 for each alloy, 3 specimens at room temperature and 3 at 1033 K. Tensile testing was conducted at a Rolls Royce approved commercial laboratory. Thermal expansion analysis was performed on a Perkin Elmer Diamond TMA as per ASTM standard E831 using a heating rate of 5 K per minute; with 3 cycles per sample. Microstructural analysis was performed on a Nikon Eclipse LV150 optical microscope (OM) and Camscan S2 scanning electron microscope (SEM). Energy Dispersive Spectroscopy (EDS) line scans were conducted on a FEI Inspect F field emission microscope. Samples for EDS were mounted, ground and polished down to 0.05 μm. OM and SEM samples were then further electro-etched in a solution of 10 g Oxalic acid in 100 ml of distilled water with an application of 6 V over 20–30 s at room temperature.

2.2. SLM process optimisation

SLM process optimisation was conducted with focus on reducing both porosity (% area) and crack density (cracks

Table 1. Nominal composition (specification) for Hastelloy X with actual composition of OHX from chemical analysis.

Element	Ni	Cr	Fe	Mo	Co	Mn	Si	W	C
Nominal (wt.%)	bal	20.5–23.0	17.0–20.0	8.0–10.0	1.5–2.5	0.2–1.0	max 1.0	0.6–1.0	0.05–0.15
OHX (wt.%)	bal	21.3 ± 0.19	19.5 ± 0.17	9.0 ± 0.12	1.04 ± 0.04	0.48 ± 0.03	0.32 ± 0.02	0.56 ± 0.03	0.057 ± 0.01

per mm^2) for OHX. Initial process parameters were based on those successfully used in other work [2]. A further set of design of experiments was created; initially to maximise density and then reduce crack density. A high density (>99.5%), or low porosity (<0.5%), had to be achieved before concentrating on cracking, as any large pores or defects would be considered equally as detrimental.

Porosity values were determined through area percentage measurements from optical micrographs of prepared samples. Crack density was determined by counts per unit area. Using an area of 0.25 mm^2 (500 × 500 μm), 20 measurements were taken from each sample, enabling a statistically safe determination of an average per mm^2 with 95% confidence level error.

3. Establishment of rapid solidification conditions and solute trapping

3.1. Process optimisation and parameter-material response relationships

Fig. 3 displays the results of the final laser power vs apparent velocity trial for porosity and crack density of OHX, where hatch spacing, focus offset and layer thickness were fixed at 90 μm, 4 mm and 20 μm respectively. Crack density, as measured in the vertical section, was reduced to 3.2 ± 1.4 cracks per mm^2; achieved with a power of 180 W, exposure time of 150 μs and point distance of 50 μm. Although loose qualitative relationships can be identified by plotting porosity against the various controllable parameters, intra-variable relationships become more difficult to define. A more general parameter 1D line energy density is instead defined.

$$\frac{Pt_{exp}}{x_{PD}} \equiv \frac{Q}{l} \tag{4}$$

where P is power of the source, t_{exp} is the exposure time, x_{PD} is the distance between points of exposure, Q is energy and l is line length. Fig. 3 shows that sample porosity has a strong relationship with energy density, whereas crack density is more dependent on laser power. This is understood if Rosenthal's model is considered, in which the temperature profile has a significantly higher dependence on laser power than beam velocity [25]. Through TGM, it is understood that steeper temperature gradients result in increased magnitudes of thermal stress and therefore increased hot cracking [4].

The microstructure consists of large columnar grains, defined only by dendrite orientation with no visible solute segregation to grain boundaries, seen in Fig. 4. Cracks are in the form expected from hot cracking; they primarily lie along the grain boundaries, as this is often the path of least resistance. Cross sections of melt tracks are visible depending on the orientation of the dendrites; this varies due to the meander scan strategy used. The depth of the light shaded melt pool areas corresponds to the 20 μm layer thickness; the dark bands are traces of melt pools in different orientations.

3.2. Establishment of rapid solidification conditions

SEM imaging, shown in Fig. 5, reveals a close packed highly columnar structure, with minimal interdendritic segregation. The cellular morphology implies either a greater thermal gradient or interface velocity than predicted. Davies et al. [26] determined a relationship between primary Dendrite Arm Spacing (DAS) λ_1 and cooling rate, given as $(\frac{\partial T}{\partial t})$, shown in Eq. (5).

$$\lambda_1 = 97 \pm 5\left(\frac{\partial T}{\partial t}\right)^{-0.36\pm0.01} \tag{5}$$

Primary DAS was measured between 0.9 and 1.2 μm. Using Eq. (5) $|\dot{T}| \sim 3 \times 105$ K/s is calculated, which is consistent with the value used in Section 1.3 and is in agreement with $V_s \leqslant 1$ m/s. As expected the isotherms mimic the melt pool trace, which occasionally form new grain boundaries that intersect the primary columnar grains. Observed, is a microstructure dominated by high aspect ratio columnar grains with smaller equiaxed type interspersed. It is noted that the smaller grains increase in number with build height, as the influence of the heat flux reduces and competitive growth becomes more dominant.

It is now assumed that D_i of a solute is of the order of the solid diffusion coefficient D_s at $T \sim T_{melt}$. Of the solutes most present in superalloys, Si is the fastest diffuser, providing an upper limit D_s of $\sim 10^{-12}$ m^2/s [27]. Taking δ to be of the order of atomic spacing, 10^{-9} m [28], a critical interface velocity $V_{critcal} \sim 0.01$ m/s is calculated, implying SLM processing lies inside the boundary of solute trapping. Microstructures from previous investigations indicate that interdendritic microsegregation does still occur [20–22,29], and solidification velocities are not sufficient to yield microsegregation free structures (plane-front growth) which occur beyond ~3 m/s [17]. It is therefore accepted that highly mobile solutes may achieve very short distance diffusion, but V_s is high enough to inhibit intergranular segregation, and there is no direct evidence to suggest otherwise. This therefore places doubt on the conclusions of Tomus et al. regarding the segregation of minor elements towards grain boundaries and the forming of brittle/weak phases as a key factor in micro-cracking. However, the result of increasing the Si and Mn content should not be ignored as it still affects the crack susceptibility, regardless of mechanism.

In order for precipitation of secondary phases to occur, there has to be sufficient concentration of diffused solute atoms in the interdendritic region. This requires additional consideration of solid state diffusion, as opposed to that at the solid–liquid interface. If solute diffusion can occur from the top of the freezing range T_{melt} to $0.5T_{melt}$, the diffusion temperature range $\Delta T_{dif} = 0.5T_{melt} = 814$ K for Hastelloy X [30]. With a cooling rate $\dot{T} = 3 \times 10^5$ K/s, the time window for diffusion $t_{dif} = 2.2 \times 10^{-3}$ s. The steady state

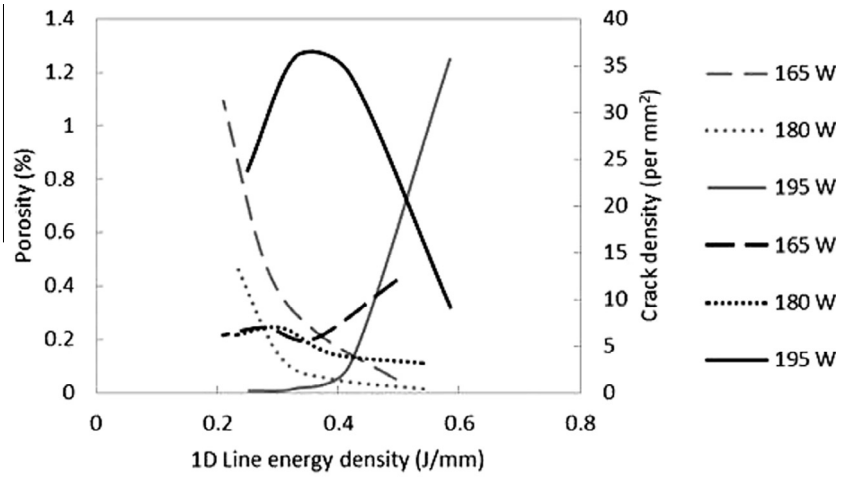

Fig. 3. Porosity (grey) and crack density (black) against 1D line energy density for final optimisation trial of OHX involving laser power varied with apparent velocity.

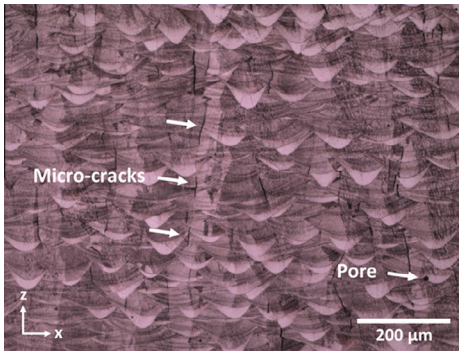

Fig. 4. Optical micrograph of etched vertical section of OHX fabricated with power of 195 W, point distance of 53 µm and exposure time of 115 µs. Sample has a crack density of 34 ± 3.5 cracks per mm^2. Note the absence of visible boundaries between grains, this is as a result of no segregation of solute to the edges of the grain and thus etching only reveals dendritic structure. Individual grains are only identifiable using a polarising filter.

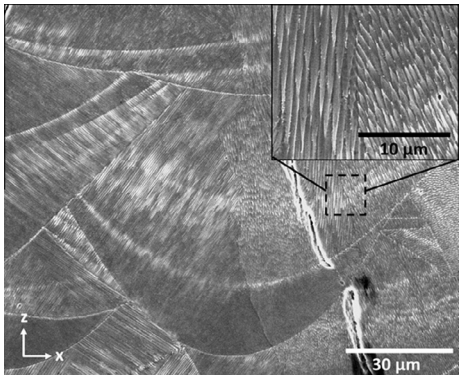

Fig. 5. SEM micrographs. Primary grain boundaries are visible running up the centre of the melt trace, a second less visible boundary is magnified in the secondary image.

diffusion distance, that is distance from the primary dendrites to the centre of the interdendritic region, $\delta_{precipitate} = \lambda_1/2 \cong 0.5 \times 10^{-6}$ m. The distance travelled by a solute atom in a time t_{dif} is given by $X = (D_s \cdot t_{dif})^{1/2}$. Using silicon again as the fastest diffuser, X(Si) $= 5.2 \times 10^{-8}$ m. The solute atoms will therefore only travel 1/10 of $\delta_{precipitate}$ before temperatures inhibit atomic movement and diffusion ceases. This implies that the required magnitude of solute diffusion for precipitation to occur, and thereby precipitation itself, would be inhibited by the solidification conditions. Observations from recent studies support this [20,22].

In the absence of additional processing (e.g. heated substrates, heat treatment and HIPing), the as deposited state of a superalloy will always be a supersaturated solid solution, with high aspect ratio columnar grains oriented in the build direction. Thus in order to affect σ_{UTS} for the as deposited condition, the solid solution strength of the alloy should be increased.

3.3. Microsegregation of minor elements

In Sections 1.1 and 3.2, it was proposed that the chemical segregation of minor elements could not be a significant factor contributing to the crack susceptibility of Hastelloy X in SLM, as rapid solidification conditions leading to solute trapping would inhibit this mechanism. To further explore this, EDS line scans were conducted across crack interfaces on a number of samples, two examples of which are displayed in Fig. 6. Inspection of the line scans indicates variation of alloying elements across the scan length; however no element is seen to significantly increase towards the crack edge, as would be expected if segregation to the grain boundary had occurred. Of particular interest is that Si, one of the minor elements highlighted by Tomus [1], does not show any sign of concentration at the crack edge, nor do any of the primary matrix elements (Ni, Cr and Fe) deplete. The only significant variation is over the crack itself, where all matrix elements dip as expected.

4. Modification of composition and crack reduction

Given the conclusions of Section 3, the increase of solid solution strength of OHX through modification of its composition is now considered.

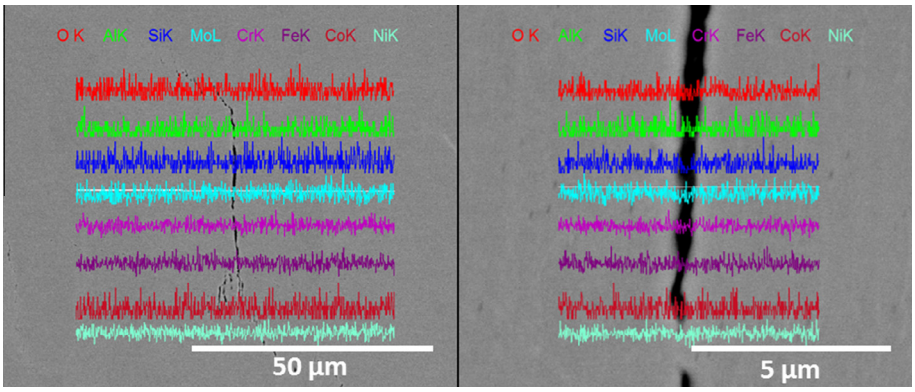

Fig. 6. Two EDS line scans of a crack at medium (left) and high (right) magnification.

4.1. Solid solution strengthening

The yield stress of a metal can be described using the Hall Petch equation.

$$\sigma_{YS} = \sigma_0 + k_d d^{\frac{1}{2}} \tag{6}$$

where σ_0 represents the lattice stress, k_d is the locking parameter value and d is the average grain size. The lattice stress can be separated to that of the solid solution contribution, σ_{ss}, and the Peierls stress σ_P.

$$\sigma_{YS} = \sigma_p + \sigma_{ss} + k_d d^{\frac{1}{2}} \tag{7}$$

We now consider the comparison of two hypothetical alloys, denoted as j and k respectively, with minor compositional variations. In order to assess $\Delta\sigma_{ss}$ processing parameters must be fixed; this then allows the following assumptions to be made. Peierls stress and k_d can be fixed as the alloy composition does not vary significantly enough and thermal conditions are identical; in addition the contribution of σ_P is minimal. As discussed in Section 1.3, grain structure is controlled by V_s and $|\dot{T}|$ which will not vary under identical processing conditions, therefore d can also be fixed. σ_{kYS}–σ_{jYS}, then reduces to $\Delta\sigma_{YS} = \Delta\sigma_{ss}$ which is then approximately equivalent to $\Delta\sigma_{UTS}$, providing ductility is not greatly affected. It is noted that this relationship holds providing the composition modification does not introduce new phases.

Gypen and Deruyttere [24] determined a model for multicomponent solid solution hardening as a function of solute concentration, when the binary Solid Solution Hardening (SSH) effect of individual solutes is known. The SSH contribution is given by:

$$\sigma_{ss} = \left(\sum_i k_i^{\frac{1}{n}} c_i\right)^n \tag{8}$$

where c_i is the concentration of solute i, and k_i is the strengthening constant of solute i. n is taken as ½ to be consistent with the dependence on concentration in Feltham's Trough model [31], as proposed by Roth et al. [31,32]. The values of k_i are determined empirically by measuring the individual strengthening contribution of the element whilst in a binary alloy. Mishima et al. [33] determined the strengthening constants for solid solution strengthening (SSS) elements in Nickel binary alloys – specific values are presented in Table 2. In the full model, a thermal component is considered but not quantified, rather assimilated into a numerical fit. In this investigation thermal contributions are accounted for in the Peierls stress.

It is not possible to determine values for total yield strength of a superalloy due to the simplicity of this model; however it will enable calculation for the difference in lattice stress as a result of minor solute concentration shifts. Therefore an alteration of the materials crack susceptibility can be achieved through the relationship $\Delta\chi = \Delta\sigma_{UTS} = \Delta\sigma_{ss}$, where

$$\Delta\sigma_{ss} = \sigma_{ssk} - \sigma_{ssj} = \left(\sum_{ik} k_i^{\frac{1}{n}} c_{ik}\right)^n - \left(\sum_{ij} k_i^{\frac{1}{n}} c_{ij}\right)^n \tag{9}$$

With j and k again representing the two alloy compositions. Before modifications are made a standard composition of Hastelloy X will be processed, and build parameters optimised to achieve the lowest possible crack density whilst maintaining full part density (>99.5%). The composition will be modified to increase the tensile strength whilst keeping the alloy within specification. The modified alloy will be processed under like for like conditions, and the crack densities will be compared to validate the hypothesis. Tensile properties and thermal expansion coefficients will also be compared to determine the validity of Eq. (9).

Table 2. Composition of MHX with elemental strengthening coefficients (k). Values for k taken from Mishima et al. [32]. The effective strengthening of each solute element can be appreciated when considering change in concentration Δc_i and solute strengthening coefficient.

Alloy	Ni	Cr	Fe	Mo	Co	Mn[a]	Si[a]	W	C
MHX wt.%	46.55 ± 0.27	21.80 ± 0.19	18.59 ± 0.17	9.40 ± 0.12	1.77 ± 0.05	0.22 ± 0.02	0.31 ± 0.02	1.05 ± 0.01	0.054 ± 0.01
OHX wt.%	47.87 ± 0.28	21.3 ± 0.19	19.5 ± 0.17	9.0 ± 0.12	1.04 ± 0.04	0.48 ± 0.03	0.32 ± 0.02	0.56 ± 0.03	0.057 ± 0.01
Δc_i (At. Frac)	−0.01	0.007	0.0004	0.003	0.007	−0.003	−0.0002	0.0016	−0.0001
k (MPa At. Fraction$^{-1/2}$)	–	337	153	1015	39.4	448	275	997	1061

[a] Considered detrimental from findings of Tomus et al. [1].

4.2. Alloy composition alterations

An independent chemical analysis of OHX powder was undertaken in order to establish the wt.% of all non-trace elements down to an accuracy of parts per million (ppm). Table 2 details the composition of the Modified Hastelloy X (MHX) as well as the associated strengthening parameters for each alloying element. In this investigation, there have been no new additions of potentially advantageous elements, as the aim is to keep the material within specification. Other alterations include a reduction of tramp elements O, N, Cu, Pd and P, which are deemed detrimental to mechanical properties of the alloy in levels down to a few ppm [34].

The increase in tensile strength as a result of the chemical manipulation $\Delta\sigma_{ss}$ was predicted to be $+8.02 \pm 1.2$ MPa. All detectable elements were included in the calculation, providing a strengthening constant existed for them.

4.3. Modified Hastelloy X: material response and property comparison

Fig. 7 displays the crack densities for MHX and OHX for a range of parameter sets, including the optimised set from Section 3.1. It is noted that the altered sample geometry, as discussed in Section 2, yielded significantly greater crack densities across the sample range due to a reduction in residual heat [35], which leads to a lower quench temperature and increased thermal gradient [4].

For this sample set, MHX yielded significantly lower crack densities in all like for like samples than the standard OHX; with an average reduction of 65% observed in the vertical section and 57% in the horizontal section. The lowest crack density measured for the MHX was 1.6 ± 0.9 cracks per mm^2, which was an 86% reduction against the equivalent OHX sample (11.6 ± 2.4 cracks per mm^2). The relatively large errors are as a consequence of the crack counting method; cracks are counted as integers and thus once crack densities reach single figure values, per cent deviation becomes large.

In order to confirm the mechanism responsible for the reduction in crack susceptibility and also validate Eq. (9), OHX and MHX were compared for tensile properties (elongation, yield strength, UTS), Young's modulus, Vicker's Hardness and thermal expansion. Tensile testing was carried out at room and elevated temperature (1033 K), see Fig. 8.

There was no discernible increase in the room temperature tensile strength of MHX, however an increase in the elevated temperature UTS was observed. UTS plus standard deviation of OHX was 484.0 ± 4.0 MPa with MHX at 500.3 ± 2.6 MPa. This is attributed to the temperature sensitivity of substitutional SSS of large solute atoms. At elevated temperatures dislocations carry a higher energy state, and the stress required to inhibit their propagation increases. At this point larger substitutional solute atoms, such as Mo and W, become more favourable as they create larger stress fields within the lattice. Their large size also inhibits their diffusion within the solid, making them a more stable barrier at elevated temperatures. This not only explains the elevated tensile results, but also reinforces the argument for increasing the atomic per cent of heavy SSS elements in favour of lighter elements such as Fe or Si to maximise TSR.

Average Vickers hardness for OHX and MHX were 277.1 ± 3.9 and 280.9 ± 4.0 $H_v0.5$ respectively. However there was great variation across the samples, due to the residual stress present, and any increase in true hardness is lost within the deviation.

Ductility of MHX was marginally higher at room temperature, and was expected due to the reduction of tramp elements, however at elevated temperature a large reduction in ductility is observed. It is proposed that the minor alterations to the composition have resulted in a shift of the critical temperature range for the elevated temperature ductility minimum of the alloy; typically around 1033 K (1400F) for nickel-base superalloys [36]. When the alloy is

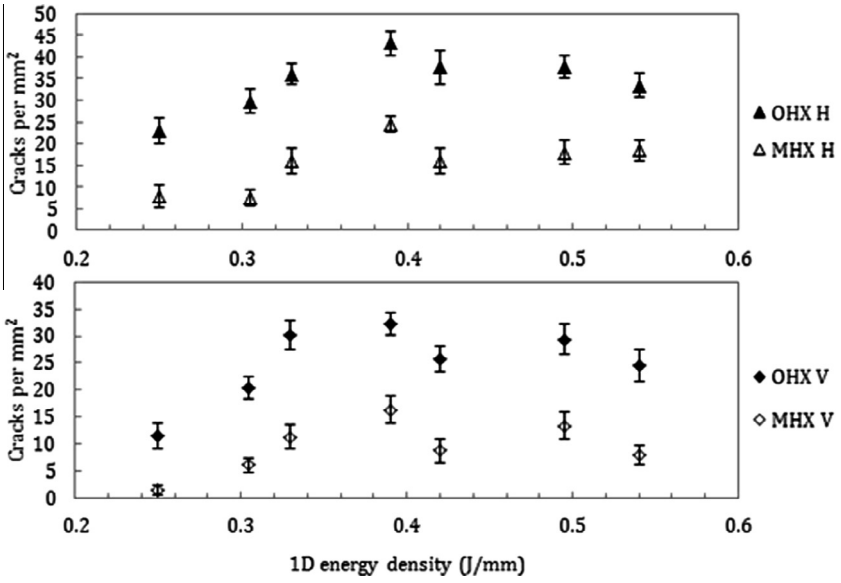

Fig. 7. Crack densities of OHX (filled) and MHX (unfilled) measured in vertical (V) build orientation, bottom plot, and horizontal (H) build orientation, top plot.

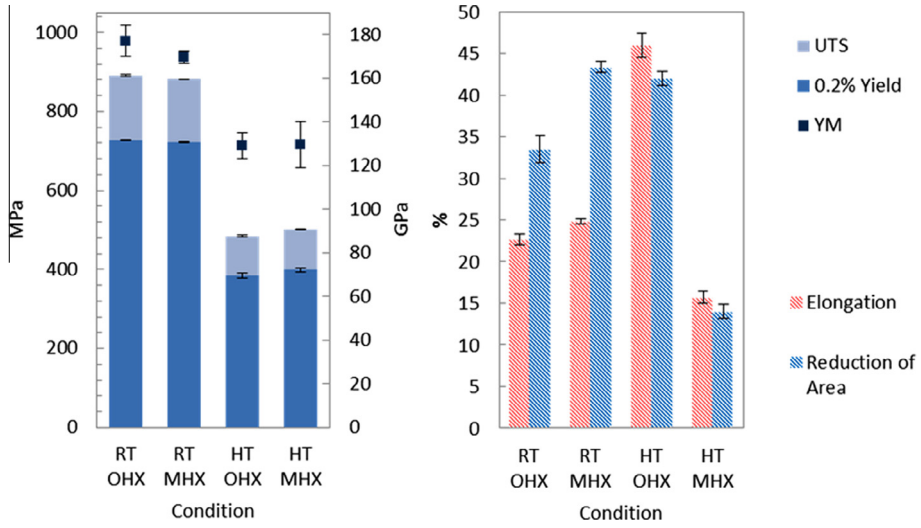

Fig. 8. Comparison of tensile properties for OHX and MHX: RT = room temperature, HT = high temperature (1033 K).

plastically deformed at temperatures approaching this minimum, it induces extensive precipitation of carbides, which deplete the SSS elements within the matrix. At the minimum, matrix strength is still sufficient to force grain boundary shear as a response to applied stress, causing extensive plastic flow which results in overall reduced ductility. Above the minimum, grain boundary shear still occurs however now the SSS elements are heavily depleted and increased bulk deformation occurs, resulting in high ductility once again [36]; as is the proposed case for OHX. Inspection of the fracture surface reveals presence of carbides for both alloys, see Fig. 9, supporting the ductility minimum for MHX. OHX displays a higher concentration of carbides than MHX, indicating more significant carbide precipitation which is consistent with its higher ductility. The authors emphasise at this point that this mechanism is not considered as a factor in micro-crack formation, as any local plastic deformation as result of thermally induced stress would not be over a sufficient range. In addition, micrographs reveal no formation of carbides in as deposited samples, see Fig. 4. The ductility minimum does pose a concern for operational life of the alloys however, and it is important that the sensitivity of this effect has been highlighted for alloy development.

The effect of composition alteration on the thermal expansion of OHX and MHX alloys is displayed in Fig. 10 and Table 3. There is no significant variation between the measured linear expansion and calculated α_{CTE} for the OHX and MHX alloys. This is expected as although Molybdenum and Tungsten have been reported to reduce α_{CTE} of Ni-base superalloys, particularly in solid solution, a significant reduction (1×10^{-6} m/K) would require increases of the order of 5 wt.% [37]. The reduction of α_{CTE}, and hence increased thermal stability, is therefore

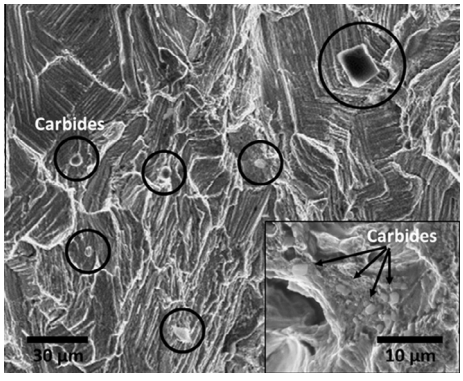

Fig. 9. Fracture surface of high temperature tensile bar for MHX (main image) and OHX (bottom corner image); black circles and arrows highlight precipitated carbides. Both alloys display small carbides which have formed as a consequence of the elevated temperature plastic deformation.

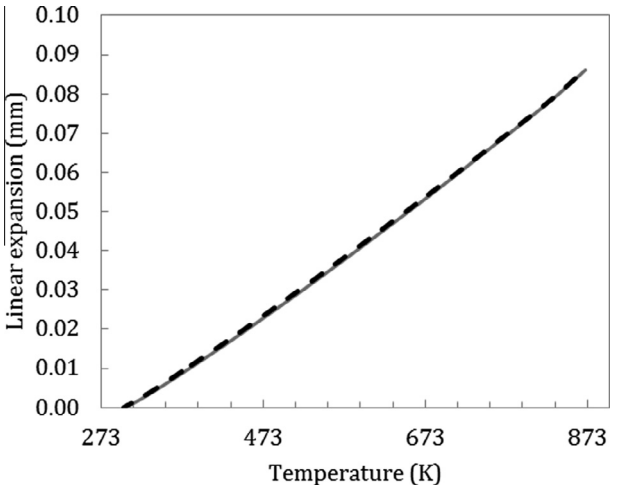

Fig. 10. Thermal expansion data for OHX (solid grey line) and MHX (dashed line) plotted as a function of temperature.

Table 3. Mean coefficient of thermal expansion for OHX and MHX alloys over full and partial temperature ranges.

Alloy	α_{CTE} (10^{-6}/K)		
	303–673 K	303–773 K	303–873 K
OHX	14.34	14.73	15.15
MHX	14.47	14.76	15.17

disregarded as a secondary mechanism responsible for the reduction of cracking in the MHX alloy.

5. Summary and conclusion

A theory for the reduction of SLM alloy crack susceptibility has been presented. It was proposed that an alloy's resistance to cracking can be improved by increasing the concentration of substitutional solid solution strengthening atoms within the lattice. From the imposed rapid solidification and process conditions, a near supersaturated solid solution with a microstructure of columnar dendrites and high aspect ratio columnar grains was predicted for the as deposited state. This proposed material condition challenged the hypothesis of previous works, which suggested that microsegregation of minor solute atoms was a major factor in the crack susceptibility of Hastelloy X in SLM processing.

After running extensive DOE for both density and minimum micro cracking, it was established that it was not possible to eliminate cracks in nominal composition Hastelloy X (OHX) through process control alone, establishing it as a candidate material to test the hypothesis. It was noted that of the controllable processing parameters, laser power had the greatest influence on crack density, whilst energy density held a stronger relationship with porosity.

The microstructures of fabricated as deposited samples were observed to be in agreement with those predicted. Structure was observed to be close packed dendritic with only primary dendrite arms visible; there was no evidence of precipitation or grain boundary segregation of solute atoms. EDS line scans of crack regions displayed no discernible variation in concentration of any matrix element across the crack or crack initiation point, thus further challenging the conclusions of Tomus et al. [1].

A modified composition of Hastelloy X (MHX) was created, in which small increases to solid solution strengthening elements and reductions in tramp elements had been made. In a direct comparison with OHX, the modified alloy displayed an average reduction in crack density of 65% in as deposited components. In concurrence, MHX also exhibited an increase in yield strength and UTS at elevated temperatures, thereby supporting the proposed theory in regard to the relationship between tensile strength and crack susceptibility. Further to this, the coefficient of thermal expansion had not been affected by the composition alteration and was therefore not regarded as a secondary mechanism for crack reduction in MHX.

Given that a significant reduction in cracking was achieved with such minor alterations to the composition, it is expected to be possible to eliminate cracks in as deposited Hastelloy X, whilst keeping it within specification. In addition, the crack reduction theory is applicable to any alloy system which forms a solid solution, allowing for future development of a range of Low Crack Susceptibility alloys for both established and novel compositions.

Acknowledgments

The authors would like to thank LPW Technology for their collaboration and material supply within this project. This work was supported by LPW Technology and the EPSRC (grant number EP/K503149/1).

References

[1] D. Tomus et al., Controlling the microstructure of Hastelloy-X components manufactured by selective laser melting, Phys. Proc. 41 (2013) 816–820.
[2] F. Wang, X.H. Wu, D. Clark, On direct laser deposited Hastelloy X: dimension, surface finish, microstructure and mechanical properties, Mater. Sci. Technol. 27 (1) (2011) 344–356.
[3] M. Zhong et al., Boundary liquation and interface cracking characterization in laser deposition of Inconel 738 on directionally solidified Ni-based superalloy, Scr. Mater. 53 (2) (2005) 159–164.
[4] P. Mercelis, J.-P. Kruth, Residual stresses in selective laser sintering and selective laser melting, Rapid Prototyping J. 12 (5) (2006) 254–265.
[5] R.J. Moat, Microstructural and residual stress characterisation of laser deposited nickel-base superalloy test structures, 2009.
[6] R.J. Moat et al., Residual stresses in laser direct metal deposited Waspaloy, Mater. Sci. Eng. A 528 (6) (2011) 2288–2298.
[7] M. Shiomi et al., Residual stress within metallic model made by selective laser melting process, CIRP Ann. Manuf. Technol. 53 (1) (2004) 195–198.
[8] F. Wang, Mechanical property study on rapid additive layer manufacture Hastelloy® X alloy by selective laser melting technology, Int. J. Adv. Manuf. Technol. 58 (5–8) (2011) 545–551.
[9] P.W. Davies, R.W. Evans, The contribution of voids to the tertiary creep of gold, Acta Metall. 13 (3) (1965) 353–361.
[10] A. Baldan, Rejuvenation procedures to recover creep properties of nickel-base superalloys by heat treatment and hot isostatic pressing techniques, J. Mater. Sci. 26 (13) (1991) 3409–3421.
[11] W.F. Savage, B.M. Krantz, Microsegregation in autogenous Hastelloy X welds, Defense Technical Information Center, 1971.
[12] J. Hunt, F. Derguti, I. Todd, Selection of steels suitable for additive layer manufacturing, Ironmaking Steelmaking 41 (4) (2014) 254–256.
[13] I. Toda-Caraballo, E.I. Galindo-Nava, P.E.J. Rivera-Díaz-del-Castillo, Unravelling the materials genome: symmetry relationships in alloy properties, J. Alloys Compd. 566 (2013) 217–228.
[14] W. Kurz, R. Trivedi, Rapid solidification processing and microstructure formation, Mater. Sci. Eng. A 179–180 (Part 1(0)) (1994) 46–51.
[15] M. Gremaud, M. Carrard, W. Kurz, The microstructure of rapidly solidified AlFe alloys subjected to laser surface treatment, Acta Metall. Mater. 38 (12) (1990) 2587–2599.
[16] M. Zimmermann, M. Carrard, W. Kurz, Rapid solidification of Al–Cu eutectic alloy by laser remelting, Acta Metall. 37 (12) (1989) 3305–3313.
[17] M. Carrard et al., About the banded structure in rapidly solidified dendritic and eutectic alloys, Acta Metall. Mater. 40 (5) (1992) 983–996.
[18] R.J. Deffley, Development of processing strategies for the additive layer manufacture of aerospace components in Inconel 718, in Department of Materials Science and Engineering, University of Sheffield, 2012.
[19] K. Amato, Comparison of microstructures and properties for a Ni-base superalloy (Alloy 625) fabricated by electron beam melting, J. Mater. Sci. Res. 1 (2) (2012) 3–41.
[20] Z. Wang et al., The microstructure and mechanical properties of deposited-IN718 by selective laser melting, J. Alloys Compd. 513 (2012) 518–523.
[21] L. Rickenbacher, High temperature material properties of IN738LC processed by selective laser melting (SLM) technology, Rapid Prototyping J. 19 (4) (2013) 282–290.

[22] T. Vilaro et al., Microstructural and mechanical approaches of the selective laser melting process applied to a nickel-base superalloy, Mater. Sci. Eng. A 534 (2012) 446–451.
[23] M.J. Aziz, Model for solute redistribution during rapid solidification, J. Appl. Phys. 53 (2) (1982) 1158–1168.
[24] L.A. Gypen, A. Deruyttere, Multi-component solid solution hardening, J. Mater. Sci. 12 (5) (1977) 1034–1038.
[25] D. Rosenthal, The theory of moving sources of heat and its application to metal treatments, Trans. ASME 68 (1946) 849–866.
[26] H.A. Davies, N. Shohoji, D.H. Warrington, The structure of rapidly quenched nickel-based superalloy ribbons produced by melt spinning, in: International Conference on Rapid Solidification Processing, 1980.
[27] P.K. Rastogi, A.J. Ardell, The coarsening behavior of the γ' precipitate in nickel-silicon alloys, Acta Metall. 19 (4) (1971) 321–330.
[28] W. Kurz, D.J. Fisher, Fundamentals of Solidification, 4th revised ed., Trans Tech Publications, Switzerland, 1998.
[29] K.N. Amato et al., Microstructures and mechanical behavior of Inconel 718 fabricated by selective laser melting, Acta Mater. 60 (5) (2012) 2229–2239.
[30] Hastelloy® X Alloy Datasheet, Haynes International Inc, 1997.
[31] P. Feltham, Solid solution hardening of metal crystals, J. Phys. D: Appl. Phys. 1 (3) (1968) 303.
[32] H.A. Roth, C.L. Davis, R.C. Thomson, Modeling solid solution strengthening in nickel alloys, Metall. Mater. Trans. A 28 (6) (1997) 1329–1335.
[33] Y. Mishima, S. Ochiai, N. Hamao, M. Yodogawa, T. Suzuki, Solid solution hardening of nickel-role of transition metal and B-subgroup solutes, Trans. Jpn. Inst. Met. 27 (9) (1986) 656–664.
[34] M.J. Donachie, S.J. Donachie, Superalloys: A Technical Guide, second ed., ASM International, Materials Park, OH, 2002, 439 p.
[35] I.A. Roberts et al., A three-dimensional finite element analysis of the temperature field during laser melting of metal powders in additive layer manufacturing, Int. J. Mach. Tools Manuf. 49 (12–13) (2009) 916–923.
[36] M.A. Arkoosh, N.F. Fiore, Elevated temperature ductility minimum in Hastelloy alloy X, Metall. Trans. 3 (8) (1972) 2235–2240.
[37] F.C. Hull et al., Effect of composition on thermal expansion of alloys used in power generation, J. Mater. Eng. 9 (1) (1987) 81–92.